



HAL
open science

Robust determination of cubic elastic constants via nanoindentation and Bayesian inference

Y. Idrissi, Thiebaud Richeton, D. Texier, S. Stéphane Berbenni, J.-S. Lecomte

► To cite this version:

Y. Idrissi, Thiebaud Richeton, D. Texier, S. Stéphane Berbenni, J.-S. Lecomte. Robust determination of cubic elastic constants via nanoindentation and Bayesian inference. *Acta Materialia*, 2024, 281, pp.120406. 10.1016/j.actamat.2024.120406 . hal-04703420

HAL Id: hal-04703420

<https://hal.science/hal-04703420v1>

Submitted on 25 Sep 2024

HAL is a multi-disciplinary open access archive for the deposit and dissemination of scientific research documents, whether they are published or not. The documents may come from teaching and research institutions in France or abroad, or from public or private research centers.

L'archive ouverte pluridisciplinaire **HAL**, est destinée au dépôt et à la diffusion de documents scientifiques de niveau recherche, publiés ou non, émanant des établissements d'enseignement et de recherche français ou étrangers, des laboratoires publics ou privés.



Distributed under a Creative Commons Attribution 4.0 International License



Full length article

Robust determination of cubic elastic constants via nanoindentation and Bayesian inference

Y. Idrissi^{a,b}, T. Richeton^{a,b,*}, D. Texier^c, S. Berbenni^{a,b}, J.-S. Lecomte^{a,b}

^a Université de Lorraine, CNRS, Arts et Métiers, LEM3, F-57000 Metz, France

^b Laboratory of Excellence on Design of Alloy Metals for low-mass Structures (DAMAS), Université de Lorraine, France

^c Institut Clement Ader (ICA) - UMR CNRS 5312, Université de Toulouse, CNRS, INSA, UPS, Mines Albi, ISAE-SUPAERO, Campus Jarlard, 81013 Albi Cedex 09, France

ARTICLE INFO

Keywords:

Nanoindentation
Bayesian inference
Elastic anisotropy
Single crystal elastic constants
Correlative micromechanics

ABSTRACT

Nanoindentation is a promising tool for advancing the estimation of single crystal elastic constants in multiphase materials. In this study, a novel protocol is presented that couples high-speed nanoindentation mapping with the Vlassak and Nix's model and Bayesian inference simulations to statistically estimate the elastic constants of cubic materials. The originality lies in considering ratios of indentation modulus as input data. For cubic elasticity, these ratios depend solely on two dimensionless parameters, which can be chosen as the Zener ratio A and the directional Poisson's ratio $\nu_{(100)}$. Using ratios mitigates the influence of experimental calibration parameters. Only two constants are varied in the Bayesian simulations, and the computation time is further reduced by employing an optimized Vlassak and Nix's model. This approach has also the great advantage to bound the search domain of $\nu_{(100)}$ and A directly from elastic stability conditions. Furthermore, the method efficiency allows for continuous variation of the uncertainty considered in the experimental moduli, leading to stabilized Bayesian inference results. The choice of the finally retained values is thus simplified, converging to the uniqueness of the single crystal elastic constants. This method is successfully applied to high-purity Ni and Inconel 718, with the predicted elastic constants aligning well with literature data.

1. Introduction

Estimating the single crystal elastic constants (SEC) of crystalline materials is a real challenge, especially when it comes to multiphase polycrystalline materials. Standard SEC characterization can involve experiments on large single crystals using classical methods such as ultrasonic wave velocities [1] or supersonic pulse echo [2]. When dealing with single-phase polycrystalline materials, inverse approaches based on micromechanical models such as the elastic self-consistent model must generally be used to identify the SEC from the macroscopic elastic constants, e.g., studies based on diffraction data [3–5]. For multiphase polycrystalline materials, the difficulty is even greater since it is very hard, if not impossible, to produce single crystals that have the exact same chemical composition that a specific phase can have within a multiphase alloy. Moreover, in this case, inverse approaches involve the development of more complex micromechanical models as the latter should take into consideration the interaction between phases [6–9].

Because it allows the probing of uniform regions regarding phase and crystallographic orientations, nanoindentation is a very promising tool to make progress in such issues. Indeed, if the indented volume

is small enough compared to the grain and phase area, a nanoindentation test can single out an elastic property, the indentation modulus E^* , that is specific to a grain crystallographic orientation [10,11]. Hence, several recent studies coupled nanoindentation tests and electron backscatter diffraction (EBSD) measurements to trace back the SEC of different materials [12–19]. However, E^* is quite different from the directional Young's modulus E^Y which can be expressed as a function of the direction \mathbf{n} as follows [20]:

$$\frac{1}{E^Y(\mathbf{n})} = S_{ijkl}n_i n_j n_k n_l \quad (1)$$

where S denotes the fourth-rank compliance tensor, \mathbf{n} is a unit-vector and the usual rule of sum over a repeated subscript is assumed. Indeed, a nanoindentation test is not uniaxial but enforces complex multiaxial stress/strain fields beneath the tip, even in elasticity [10,11,21,22]. Hence, the link between the SEC and the indentation modulus E^* is not obvious in anisotropic elasticity. The latter relationship can be achieved thanks to accurate but time-consuming finite element simulations [12–14] or through semi-analytical micromechanical models like the one of Vlassak and Nix [23–25]. The latter is based on the surface Green's

* Corresponding author at: Université de Lorraine, CNRS, Arts et Métiers, LEM3, F-57000 Metz, France.

E-mail address: thiebaud.richeton@univ-lorraine.fr (T. Richeton).

function derived by Barnett and Lothe [26] within the Stroh formalism [27]. Still because of multiaxiality, the anisotropy displayed by E^* is actually much more reduced than the anisotropy of the directional Young's modulus (e.g., for Ni, E^Y can double from one orientation to the other while E^* varies at most by 10% [10]). Given the uncertainty in the measurement of E^* , this reduced anisotropy can be critical for many materials to have well-defined variations of E^* with grain orientations measured by EBSD. Statistical approaches, like Bayesian inference, are therefore recommended to improve the robustness of the method of elastic constants determination and take into consideration the experimental uncertainties [13,14].

In the present study, a novel protocol is presented that couples nanoindentation tests with the Vlassak and Nix's model and Bayesian inference simulations to statistically estimate the elastic constants of cubic materials. The originality lies in considering ratios of indentation modulus E^* as input data. The interest is that these ratios just depend on two dimensionless parameters, the Zener ratio A and the directional Poisson's ratio $\nu_{(100)}$ of which limits are well-known and material's independent. As it will be detailed in the manuscript, this approach has many other advantages. In the first place, the computation time is greatly reduced by considering two constants instead of three and also by using the Vlassak and Nix's model. Computing E^* from this model turns out to be far much faster than running finite element simulations. It also avoids the need to develop surrogate models based on finite element simulations [13,14]. Indeed, once its numerical implementation has been optimized, the Vlassak and Nix's model is very efficient and provides fast results ($\ll 1$ s, see further Section 3). Furthermore, it is acknowledged that this model is very accurate since it agrees very well with predictions obtained by the finite element method in linear elasticity at relatively small depth [14,28] or with predictions of molecular dynamics simulations [29].

The paper is organized as follows. Section 2 first present the experimental methodology consisting in a coupling between EBSD measurements and high-speed nanoindentation mapping (HSNM) [30] with a Berkovich tip in continuous stiffness measurement (CSM) mode under displacement control. It is applied on two different cubic materials: high-purity Ni of which elastic constants are well documented in the literature and the superalloy Inconel 718 of which SEC values are much less well known. In Section 3, a description of the Vlassak and Nix's model [23–25] and its numerical implementation are provided. The originality of our approach is detailed in Section 4. After a quick description of the Bayesian inference theory, its application to the Vlassak and Nix's model and nanoindentation measurements through our original coupling is presented. Moving on to Section 5, the results from the correlative mechanical microscopy analyses and the Bayesian inference simulations are shown. Section 6 then turns to a discussion of these results, with a specific focus on comparisons with SEC data from the literature.

2. Materials and experimental procedure

2.1. Materials

Two different materials were considered for this study: a high-purity (99.99%) nickel (Ni) provided by *GoodFellow* and a wrought Inconel 718 (IN718). For the high-purity Ni, a heat treatment at 900 °C for 2 h was first conducted to eliminate any residual constraints stemming from the casting process. The IN718 alloy was provided as a rolled plate in solid solution state. The chemical composition of the IN718 was Ni–18.5Cr–18.3Fe–5.0(Nb+Ta)–3.0Mo–1.0Ti–0.6Al–0.03C (wt. %). The sample was given a 5 min heat treatment at 1080 °C followed by water quenching to favor grain growth and recrystallization for minimal grain orientation spread. A 720 °C–8 h–cooling 50 °C.h⁻¹ + 620 °C–8 h–furnace cooling was applied to precipitate L1₂- γ' -Ni₃(Ti,Al) and DO₂₂- γ'' -Ni₃Nb phases within the γ -Ni matrix. Phases distribution and sizes were too narrow and small for this material to be evaluated individually using nanoindentation.

2.2. Sample preparation

Sample preparation is a crucial and critical step for nanoindentation testing. Ensuring the accuracy and repeatability of results hinges on the meticulous preparation of the sample surface. Both materials experienced similar surface preparation procedures. The surface preparation consisted in mechanical polishing using a precision jig with grit paper down to P4000 grit size to ensure flatness, parallelism and minimal work-hardening of the surface [31]. Manual polishing using diamond particles from 3 μ m down to 0.25 μ m aimed at limiting scratches. The surface finish consisted in a manual mechanical polishing during 20 min followed by a vibratory polishing for 3 h using a colloidal silica solution (0.05 μ m particles). This surface finish was necessary for EBSD characterizations and nanoindentation testing. A particular care was given to the surface cleaning to avoid particle contamination at the sample surface.

2.3. EBSD characterization

For the Ni sample, EBSD characterizations were performed with a step size of 5 μ m and a field of view of 3.9 \times 4.8 mm using a JEOL JSM 6490 scanning electron microscope equipped with a tungsten filament and an Oxford Instruments Symmetry S2 EBSD acquisition system. For the IN718 material, EBSD characterizations were performed with a step size of 0.4 μ m and a field of view of 1.0 \times 1.0 mm using a JEOL JSM 7100F scanning electron microscope that is also equipped with a Symmetry S2 EBSD detector (Oxford Instruments). EBSD data were post-treated and plotted using MTEX [32] and the open source Pymicro library¹ [33] for further correlative mechanical microscopy [34].

2.4. High speed nanoindentation mapping

High speed nanoindentation mapping (HSNM) was performed with a diamond-type Berkovich tip on both materials using a customized FTI04 and a NMT04 nanoindentation system both from Femtotools^{AG} for the pure Ni and the IN718 samples, respectively. This choice was made due to “point-and-shoot” options not available on the NMT-04, but necessary for the large Ni sample in order to position the indents within the previously performed EBSD map. Tests were conducted in continuous stiffness measurement (CSM) mode under displacement control allowing for similar indentation depths from indent to indent, regardless of the local mechanical response. The indentation parameters were adapted to the material to avoid stress drops due to activation of an intense plastic event (see Table 1 summarizing all the nanoindentation parameters). The CSM mode corresponds to a dynamic test in which the sample is loaded with a cyclically applied increasing penetration depth. The mass of the FTI-04 system being greater than the one of the NMT-04 system, the resonance frequency of the NMT-04 system is higher, allowing HSNM at higher CSM frequency for the IN718 alloy (see Table 1). The CSM mode was chosen in order to better evaluate the indentation modulus from statistical data as it allows the possibility to reach a stabilized modulus as a function of the depth. A 20 mN load cell with a position noise floor ± 0.05 nm and a load noise of ± 0.05 μ N (MEMS sensor) was used. The Berkovich tip was calibrating using a fused silica with isotropic elastic properties and known indentation modulus in displacement-controlled mode. For the fused silica, the values of the reduced (or effective) modulus E_R stabilized for contact depth h_c ranging from 20 to 300 nm.

The different steps to measure the anisotropic indentation modulus E^* in CSM mode is explained briefly in the following. The displacement of the tip $h(t)$ oscillates at the CSM frequency f_{CSM} . Under the assumption of small amplitude oscillations, this generates an oscillating force $F(t)$ with a phase shift angle ϕ in a linear approximation [35].

¹ <https://github.com/heprom/pymicro>.

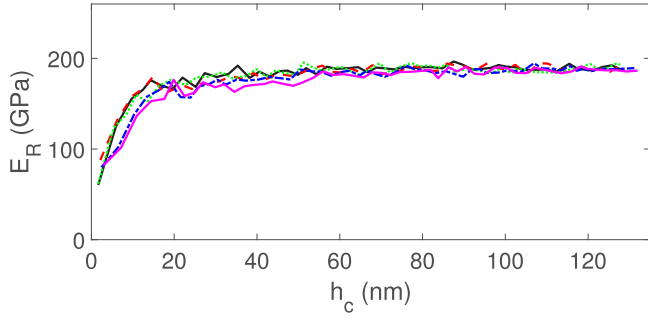


Fig. 1. Examples of variation of the reduced modulus E_R with the contact depth h_c for 5 indents in a same grain of the IN718 sample.

Table 1

Nanoindentation parameters in CSM and displacement control mode.

	Ni	IN718
Array size (indents)	400 × 250	300 × 300
Step size (μm)	10.0	2.0
CSM frequency (Hz)	50	200
Max depth (nm)	120	120
Load rate (nm s ⁻¹)	100	90
Displacement amplitude (nm)	const. 3	const. 5
Approach wait (s)	0.2	0.1
Unload time (s)	0.02	0.02
Trigger force (μN)	10	20
Frame stiffness (N m ⁻¹)	24 372.0	10 624.3

The stiffness S of the sample at each cycle can then be related to ϕ as follows [36]:

$$S = \frac{\Delta F}{\Delta h} \cos \phi \quad (2)$$

where ΔF is the load amplitude and Δh the displacement amplitude. Please note that, for more clarity, the effects of frame stiffness and mass of the instrument are not included in Eq. (2). Besides, the reduced modulus E_R is related to S as [37]:

$$E_R = \frac{\sqrt{\pi}}{2\beta} \frac{S}{\sqrt{A_p}} \quad (3)$$

β is a tip shape geometric descriptor ($\beta = 1.034$ for a Berkovich tip) and A_p is the projected area of contact which is a calibrated function of the contact depth h_c . As a result, a variation of E_R with respect to h_c is obtained. E_R tends to a stabilized behavior as depth increases, as it can be observed in Fig. 1. A single value of E^* was then evaluated for each measurement point using the average value for contact depths between 80 and 120 nm. At the end, the values of E^* were deduced from the following general relation for an anisotropic elastic material [11,24,38]:

$$\frac{1}{E_R} = \frac{1}{E^*} + \frac{1 - \nu_i^2}{E_i} \quad (4)$$

where $\nu_i = 0.07$ and $E_i = 1141$ GPa denote the Poisson's ratio and the Young's modulus of the isotropic diamond indenter, respectively.

For the high-purity Ni sample, a map of 400 × 250 indents was made with a step size of 10 μm. For the IN718 sample, a map of 300 × 300 indents was made with a step size of 2 μm. The step size was fixed in order to adapt to the sample's grain size. The microstructure of the Ni sample being coarser (mean grain size of 203 μm) than the one of the IN718 alloy which contains a lot of thin twins (mean grain size of 38 μm considering the twins, see also Fig. 3), the step size was greater. Based on the noise floor for displacement and force channels, a linear regression between 1 and 30 μN was used from the force vs. displacement curve to estimate the contact point for each measurement point as the interception between the regression line and the abscissa.

After performing the high speed nanoindentation mapping, correlative mechanical microscopy analyses were conducted using both EBSD measurements and nanoindentation responses (see Ref. [19] for more details). Non-rigid registration of the EBSD maps was performed in order to affect orientation information for each nanoindentation measurement. Grains were segmented and labeled. Grain erosion was carried out in such a way as to take into account only nanoindentation tests carried out more than 4 μm away from a grain boundary. A sampling mask was also applied on the IN718 data to remove indents located in carbides, identified both on backscattered electron images and indentation maps (high hardness and stiffness). Average values per grain of E^* along with standard deviations were subsequently computed. In total, 158 and 176 grains were available for the high-purity Ni and the Inconel 718 samples, respectively. However, for the Bayesian simulations, only large grains having a standard deviation on E^* lower than 12 GPa were kept. The purpose of this approach was to increase even more the robustness of the input data by ensuring that average values of E^* result mostly from indents far way from grain boundaries. Considering the difference of grain size and step size between the two samples (see Table 1), grains with equivalent diameter greater than 100 μm and 6 μm were selected for the Ni and IN718 samples, resulting in reduced numbers of 57 and 69 grains used in the Bayesian simulations, respectively.

3. Vlassak and Nix's model based on Stroh matrix formalism

3.1. Original theory

Vlassak and Nix [23–25] developed a theory which can evaluate E^* for a given crystallographic orientation and a set of elastic constants. It is based on the surface Green's function derived by Barnett and Lothe [26] within the Stroh formalism [27]. Assuming that the indenter geometry corresponds to a circular flat punch, Vlassak and Nix [23–25] have shown that E^* can be computed as:

$$E^* = 4\pi \left(\int_0^{2\pi} n_i B_{ij}^{-1}(\omega) n_j d\omega \right)^{-1} \quad (5)$$

where \mathbf{n} is the unit normal to the indentation surface in the crystal's coordinate system which is related to the Euler angles of a given orientation. \mathbf{B} is a symmetric matrix that depends on the anisotropic elastic tensor \mathbf{C} . \mathbf{B} was originally expressed as a line integral within the Stroh integral formalism [23–25]:

$$B_{ij} = \frac{1}{2\pi} \int_0^{2\pi} \left((mm)_{ij} - (mn)_{ik} (nn)_{kp}^{-1} (nm)_{pj} \right) d\omega \quad (6)$$

where the tensor \mathbf{C} is included in the notation $(mn)_{jk} = m_i C_{ijkl} n_l$. The vector \mathbf{m} is obtained as $\mathbf{m} = \mathbf{n} \wedge \mathbf{t}$ where \mathbf{t} is an arbitrary unit vector in the plane perpendicular to \mathbf{n} . It makes an angle ω with a fixed datum of the plane perpendicular to \mathbf{n} . ω corresponds to the angle that varies from 0 to 2π in the line integral of Eq. (5).

3.2. Stroh matrix formalism

The matrix \mathbf{B} can however be computed more efficiently using the Stroh matrix (or sextic) formalism (see, e.g., Refs. [10,27,39–41]) which needs first to solve an eigenvalue problem:

$$\mathbf{N} \xi^\alpha = p_\alpha \xi^\alpha \quad (7)$$

where p_α denotes the six eigenvalues of the matrix \mathbf{N} . \mathbf{N} is a 6 × 6 matrix related to \mathbf{C} and given by:

$$\mathbf{N} = - \begin{bmatrix} (nn)^{-1} (nm) & (nn)^{-1} \\ (mn) (nn)^{-1} (nm) - (mm) & (mn) (nn)^{-1} \end{bmatrix} \quad (8)$$

The six eigenvalues p_α appear in the form of 3 pairs of complex conjugates [27,39–41]. By convention, $p_{i+3} = \bar{p}_i$ and $\text{Im}(p_i) > 0$ for

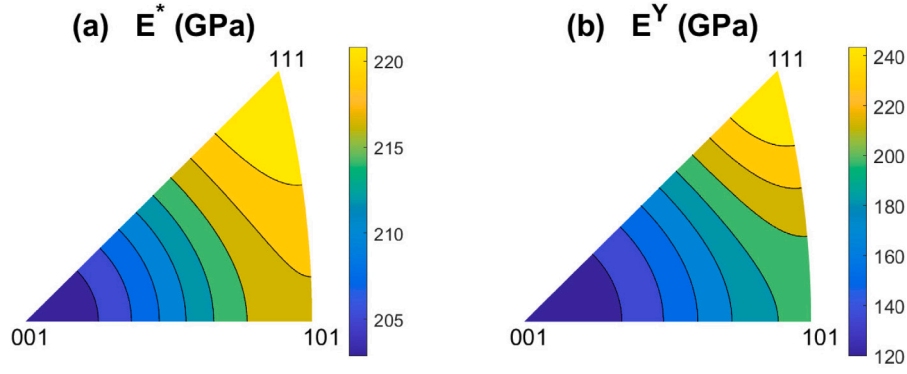


Fig. 2. IPF contour along the indentation direction of (a) E^* computed from Eq. (5) and (b) of E^Y the directional Young's modulus along the indentation axis. The Ni cubic elastic constants of [42] were considered: $C_{11} = 244$ GPa, $C_{12} = 158$ GPa and $C_{44} = 102$ GPa.

$i = 1$ to 3. ξ^α are the eigenvectors that are split into two 3×1 column vectors as:

$$\xi^\alpha = \begin{bmatrix} A^\alpha \\ L^\alpha \end{bmatrix} \quad (9)$$

A^α and L^α are then normalized according to the relation:

$$\sum_{i=1}^3 A_i^\alpha L_i^\beta + A_i^\beta L_i^\alpha = \delta_{\alpha\beta} \quad (10)$$

Finally, the matrix B is obtained as:

$$B_{ij} = 2i \sum_{\alpha=1}^3 L_{i\alpha} L_{j\alpha} \quad (11)$$

3.3. Numerical application

A Gauss–Legendre quadrature method is used to solve the line integral of Eq. (5). An accuracy of 10^{-4} % is reached with 30 integration points. In combination with the use of the matrix formalism, this results in negligible computation times to get E^* ($\ll 1$ s).

The above theoretical framework is rigorously valid for a circular contact area. Even for a spherical indenter, the contact area with an anisotropic half-space is actually only circular for surfaces with high symmetry like (111) or (100) surfaces in cubic symmetry [23–25]. Otherwise, the contact area is elliptic. However, the resulting difference in E^* value is definitely well below the experimental scatter of a nanoindentation experiment (see, e.g. Fig. 1).

For an indenter with a triangular shape like a Berkovich tip, E^* depends on the orientation of the indenter in the indentation surface. Vlassak and Nix [24] have shown that these variations are very small and can also be reasonably neglected considering the experimental scatter. However, they have also shown that the indentation moduli for triangular indenter are on average 6% higher than the corresponding moduli for axisymmetric indenter [24]. Hence, a corrective multiplicative factor of 1.06 is considered in this work to evaluate E^* for a Berkovich tip, as was done by Aspinall et al. [17].

Using this model and C_{ij} constants from the literature [42], the inverse pole figure (IPF) of the theoretical E^* for high-purity Ni can be computed (see Fig. 2), showing similar results as Li et al. [10]. For comparison, the IPF of the directional Young's modulus E^Y along the indentation axis is also plotted in Fig. 2. Indeed, it is important to show how E^Y can be different from E^* since, unfortunately, it happens that both quantities are still confused in the literature. The most noticeable difference is the relative restricted range of E^* values: while the maximum value of E^Y is more than twice the minimum value, the maximum value of E^* is only about 10% higher than the minimum value.

4. Bayesian inference

4.1. Theory

Bayesian inference is an advanced statistical method based on Bayes' theorem. One advantage of this approach is its ability to integrate prior knowledge and beliefs in the analysis. It also manages the inherent uncertainties in the observations. As a result, model parameters come also with uncertainties, thus providing a probabilistic framework that enables a more nuanced understanding and interpretation of the estimations, surpassing traditional methods that lacks context [43]. For instance, Bayesian inference was recently used in combination with the standard linear solid model and different mechanical tests to identify viscoelastic material parameters [44] or in combination with reduced-order finite-element models and spherical nanoindentation experiments to identify SEC [14]. In [9], it was used in combination with high energy X-ray diffraction measurements and an elastic self-consistent model (ELSC) to identify SEC. It was found that considering grain morphology in the ELSC model had an important effect on the determination of the SEC with this method. In the present study, a simplified Bayes theorem is evaluated as follows [45]:

$$P(A|B) = \frac{P(B|A)P(A)}{P(B)} \quad (12)$$

where $P(A|B)$ is called the posterior probability. It is the probability that the hypothesis A is true given that the evidence B has occurred. $P(B|A)$ is called the likelihood. It is the probability of observing the evidence B given that the hypothesis A is true. $P(A)$ is the prior belief which is the probability of A being true before observing B . $P(B)$ is the probability of observing the evidence B . $P(B)$ can be calculated by integrating over all possible values of A :

$$P(B) = \int_A P(B|A) dA \quad (13)$$

$P(B)$ is also often discarded as a normalization factor [9,14,44], but for some non-trivial models, $P(B)$ can be extremely difficult to estimate in a closed-form way.

4.2. Application to Vlassak and Nix's model and nanoindentation measurements

Regarding the Vlassak and Nix's model, an interesting feature comes to light by noticing that any term present as a pre-factor in the stiffness tensor C also appears as a pre-factor in the indentation modulus E^* . In the crystal's coordinates system and using Voigt notation, the cubic stiffness matrix C is usually written with respect to the three classical

constants C_{11} , C_{12} and C_{44} as:

$$C = \begin{bmatrix} C_{11} & C_{12} & C_{12} & 0 & 0 & 0 \\ C_{12} & C_{11} & C_{12} & 0 & 0 & 0 \\ C_{12} & C_{12} & C_{11} & 0 & 0 & 0 \\ 0 & 0 & 0 & C_{44} & 0 & 0 \\ 0 & 0 & 0 & 0 & C_{44} & 0 \\ 0 & 0 & 0 & 0 & 0 & C_{44} \end{bmatrix} \quad (14)$$

However, in our case, it is actually more beneficial to write C as (see the justification in Appendix):

$$C = \frac{E_{\langle 100 \rangle}}{(1 + \nu_{\langle 100 \rangle})(1 - 2\nu_{\langle 100 \rangle})} \times \begin{bmatrix} 1 - \nu_{\langle 100 \rangle} & \nu_{\langle 100 \rangle} & \nu_{\langle 100 \rangle} & 0 & 0 & 0 \\ \nu_{\langle 100 \rangle} & 1 - \nu_{\langle 100 \rangle} & \nu_{\langle 100 \rangle} & 0 & 0 & 0 \\ \nu_{\langle 100 \rangle} & \nu_{\langle 100 \rangle} & 1 - \nu_{\langle 100 \rangle} & 0 & 0 & 0 \\ 0 & 0 & 0 & A \frac{1-2\nu_{\langle 100 \rangle}}{2} & 0 & 0 \\ 0 & 0 & 0 & 0 & A \frac{1-2\nu_{\langle 100 \rangle}}{2} & 0 \\ 0 & 0 & 0 & 0 & 0 & A \frac{1-2\nu_{\langle 100 \rangle}}{2} \end{bmatrix} \quad (15)$$

where $E_{\langle 100 \rangle}$ and $\nu_{\langle 100 \rangle}$ are, respectively, the Young's modulus and the Poisson's ratio considering a uniaxial test along a $\langle 100 \rangle$ crystallographic direction, whereas A is the Zener ratio defined as the ratio of μ'' over μ' , the $\{001\}\langle 100 \rangle$ and $\{001\}\langle 110 \rangle$ shear resistances of the crystal (e.g., see [46]), respectively:

$$A = \frac{\mu''}{\mu'} = \frac{2C_{44}}{C_{11} - C_{12}} \quad (16)$$

Indeed, from this notation of C , it becomes clear that ratios of E^* computed from Eq. (5) depend on only two dimensionless elastic parameters which can be taken as A and $\nu_{\langle 100 \rangle}$. This finding proves to be very useful when performing Bayesian inference. As a matter of fact, the computation time is greatly reduced by varying 2 parameters instead of 3. In addition, from Born's elastic stability conditions, the limits of $\nu_{\langle 100 \rangle}$ and the lower limit of A are well-known and material's independent: $0 < \nu_{\langle 100 \rangle} < 0.5$ and $A > 0$ whereas the upper limit of A can be easily conjectured ($A < 15$) or adjusted rapidly if necessary on the basis of a first Bayesian simulation. On the contrary, the bounds of the C_{ij} constants for an unknown material are far much harder to estimate a priori [9]. Hence, the present approach presents a huge advantage compared to classical ones which necessitate several Bayesian simulations just to define the correct bounds of a given material. On top of that, the use of ratios increases the number of input data: $n(n-1)/2$ independent ratios for n values of E^* and also mitigates the influence of the various parameters needed to be calibrated for a nanoindentation test, such as the projected contact area function. Indeed, considering two measurements (1) and (2) at a same contact depth, the ratio of indentation moduli can be expressed from Eqs. (3) and (4) as:

$$\frac{E^{*(1)}}{E^{*(2)}} = \frac{\frac{S^{(1)}}{S^{(2)}} - (1 - \nu_i^2) \frac{E_R^{(1)}}{E_i}}{1 - (1 - \nu_i^2) \frac{E_R^{(1)}}{E_i}} \quad (17)$$

From this equation, it becomes clear that the ratios of indentation moduli depend mainly on the measured stiffness ratios while the influence of the geometrical parameter β and of the calibrated projected contact area A_p involved in the expression of the reduced modulus $E_R^{(1)}$ (cf. Eq. (3)) is negligible since $E_i \gg E_R^{(1)}$.

In our Bayesian framework, Bayes' theorem is thus applied as follows:

$$P((A, \nu_{\langle 100 \rangle}) | R^*) = \frac{P(R^* | (A, \nu_{\langle 100 \rangle})) P((A, \nu_{\langle 100 \rangle}))}{P(R^*)} \quad (18)$$

R^* denotes the $m = n(n-1)/2$ independent ratios computed from the n experimental E^* values. A given ratio, denoted as R_j^i or R_k , is

simply defined as:

$$R_k = R_j^i = \frac{E_i^*}{E_j^*} \quad (19)$$

For the Bayesian inference simulations, we consider only one E_i^* value per grain (see Section 2.4). The corresponding standard-deviation is denoted $\sigma_{E_i^*}$. Considering a normal approximation, the standard-deviation of the ratio distribution can then be estimated as [47]:

$$\sigma_{R_j^i} = \frac{E_i^*}{E_j^*} \sqrt{\frac{\sigma_{E_i^*}^2}{E_i^{*2}} + \frac{\sigma_{E_j^*}^2}{E_j^{*2}}} \quad (20)$$

In Eq. (18), $P(R^* | (A, \nu_{\langle 100 \rangle}))$ is the likelihood and stands for the probability of observing all the ratios R^* for a given couple $(A, \nu_{\langle 100 \rangle})$. It is computed as:

$$P(R^* | (A, \nu_{\langle 100 \rangle})) = \prod_{k=1}^m P(R_k | (A, \nu_{\langle 100 \rangle})) \quad (21)$$

It is noteworthy that log-probabilities are actually used in the computational framework for numerical stability. $P(R_k | (A, \nu_{\langle 100 \rangle}))$ is evaluated by comparing the experimental value of R_j^i to the ratio r_j^i obtained from the Vlassak and Nix's model (Eq. (5)) considering the Euler angles of the two grains and the tested values of A and $\nu_{\langle 100 \rangle}$. Concretely, a normal distribution centered around R_j^i and of variance $\sigma_{R_j^i}^2$ is created while the interval $[0, 3\sigma_{R_j^i}]$ is discretized into 100 bins. The likelihood corresponds to the probability of the absolute difference $|r_j^i - R_j^i|$ to fall within a given bin. If $|r_j^i - R_j^i|$ does not fall within any of the created bins, then the likelihood corresponds to the probability of $|r_j^i - R_j^i|$ to be greater than $3\sigma_{R_j^i}$.

At the end of the Bayesian inference procedure, $P(R^*)$ serves as a normalization factor to come back from log-probabilities to the classical probabilities defined within the usual $[0, 1]$ interval. The procedure thus provides as an output $P((A, \nu_{\langle 100 \rangle}) | R^*)$ which is the probability distribution that the values of the couple $(A, \nu_{\langle 100 \rangle})$ are correct given the observations of the indentation modulus ratios R^* . From this posterior probability distribution, one can easily obtain, through summations, $P(A | R^*)$ the marginal probability distribution that the values of A are correct given the observations of R^* , as well as $P(\nu_{\langle 100 \rangle} | R^*)$ the marginal probability distribution that the values of $\nu_{\langle 100 \rangle}$ are correct given the observations of R^* .

On the other hand, the posterior probability distribution $P(E_{\langle 100 \rangle} | R^*)$ can be obtained directly by simple allocations of the probabilities $P((A, \nu_{\langle 100 \rangle}) | R^*)$. The relevant value of $E_{\langle 100 \rangle}$ which should be associated with a given couple $(A, \nu_{\langle 100 \rangle})$ can indeed be evaluated as the median of the ratios distribution between experimental indentation moduli E_i^* and normalized theoretical moduli. The latter are obtained, for each grain, from the Vlassak and Nix's model considering $E_{\langle 100 \rangle} = 1$ and the tested couple $(A, \nu_{\langle 100 \rangle})$.

For both samples, no *a priori* knowledge is considered for the values of A and $\nu_{\langle 100 \rangle}$. The range of A and $\nu_{\langle 100 \rangle}$ values simply follows the Born's elastic stability conditions and the choice of a very high upper limit for A (15):

$$0 < A < 15 \text{ and } 0 < \nu_{\langle 100 \rangle} < 0.5 \quad (22)$$

In order to run the Bayesian simulations, evenly spaced values of A and $\nu_{\langle 100 \rangle}$ within the above ranges are hence considered with the exact same total number of A and $\nu_{\langle 100 \rangle}$ values. This procedure amounts to assume a uniform distribution for the prior belief $P((A, \nu_{\langle 100 \rangle}))$. To perform the Bayesian simulations, one needs also to define the values of $\sigma_{E_i^*}$. The latter could be estimated from the standard-deviations associated to the distributions of measured indentation moduli in a same grain. However, such values do not account for the uncertainties related to the EBSD measurements, to the linear approximation in the analysis of the oscillatory indentations [35] and to the tip and device

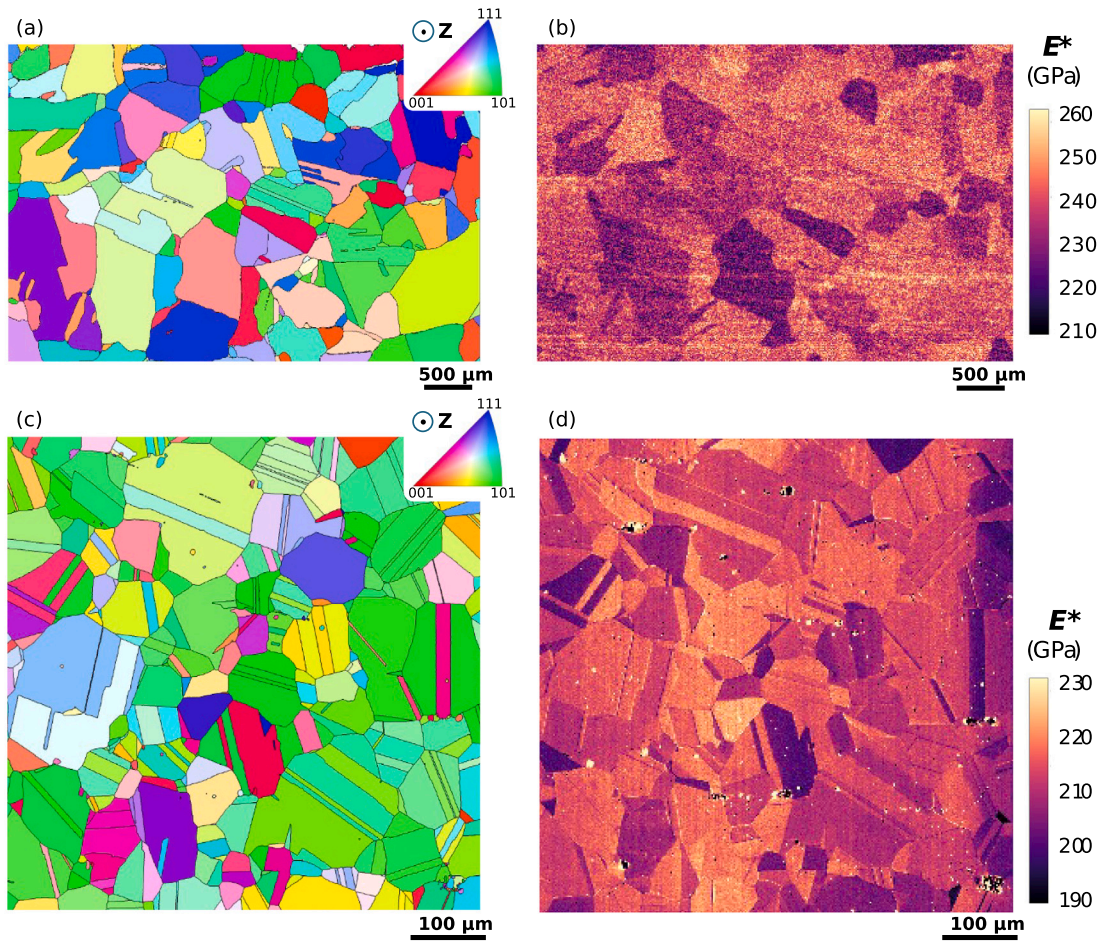


Fig. 3. EBSD inverse pole figures of the Ni (a) and IN718 (c) samples along the indentation direction and corresponding maps of indentation modulus E^* within the same area (Ni (b) and IN718 (d)).

calibrations which are fixed before performing the nanoindentation mapping. Furthermore, it accounts only partially for the uncertainties due to the sample's surface preparation, the detection of the contact point or the effect of environment (temperature, vibrations, etc.). Instead, a fixed value of σ_{E^*} is therefore rather considered for all the grains herein. Since such a value of σ_{E^*} is actually not well-known, the value of σ_{E^*} is varied continuously, which is possible thanks to the quickness of the present approach, in order to investigate its effect on the posterior probability distributions. Varying the standard deviations allows more flexibility in how the experimental data is interpreted, helping the Bayesian simulation achieve a more stable and robust convergence. This approach can also unravel the choice of the final retained constants by looking for stabilized values.

Besides, for comparison purposes, the R^2 score (or coefficient of determination) is also computed for each tested couple $(A, v_{(100)})$ as:

$$R^2(A, v_{(100)}) = 1 - \frac{\sum_k (R_k - r_k(A, v_{(100)}))^2}{\sum_k (R_k - \bar{R})^2} \quad (23)$$

where \bar{R} denotes the mean of the experimental ratios and r_k the ratio obtained from the Vlassak and Nix's model. The R^2 score increases when the least-square error, i.e. the sum of the squared differences between experimental and theoretical ratios, decreases.

5. Results

5.1. Results from the correlative mechanical microscopy

We first present results from the correlative mechanical microscopy analyses, i.e., how the nanoindentation measurements are correlated to the crystallographic orientations obtained by EBSD. Regarding this issue, Fig. 3 shows side-by-side EBSD inverse pole figures according to the nanoindentation direction and maps of E^* within the same area for the two samples. From Fig. 3, it can be observed that the shape of almost all the grains of the IN718 sample can be retrieved from the map of E^* . The map is very clear with well-defined grains. For the Ni sample, the map of E^* is more blurred, probably mainly because the surface finish was not as good as for the IN718 sample. The fact of having worked on a larger map with a lower spatial resolution and a lower CSM frequency (see Table 1) with a different nanoindentation system certainly also played a role. Nevertheless, a majority of grains can still be clearly identified. As expected from theoretical calculations in face-centered-cubic (fcc) structures with Zener ratio greater than one (see, e.g., Fig. 2), the softest and stiffest grains correspond to grains with orientations nearly aligned with $\langle 100 \rangle$ (red grains) and $\langle 111 \rangle$ (blue grains), respectively.

In addition, the average values per grain of E^* selected for the Bayesian inference simulations according to the procedure detailed in Section 2.4 are plotted in an inverse pole figure along the indentation direction for the two samples in Fig. 4. This figure shows the relevance of our approach, with a variation of E^* which is globally consistent with the theoretical IPF map of Fig. 2.

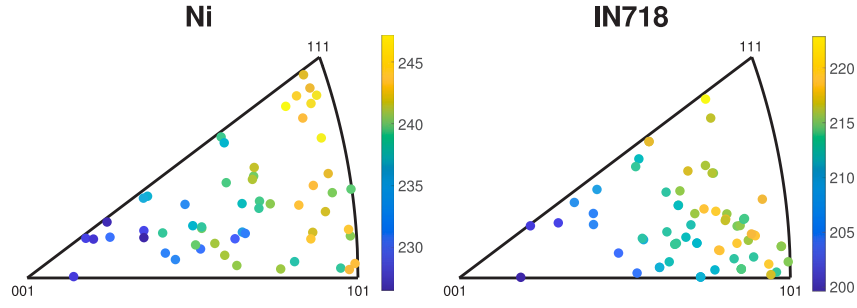


Fig. 4. Experimental average values per grain of E^* (in GPa) considered in the Bayesian inference simulations plotted in an inverse pole figure along the indentation direction for the two samples.

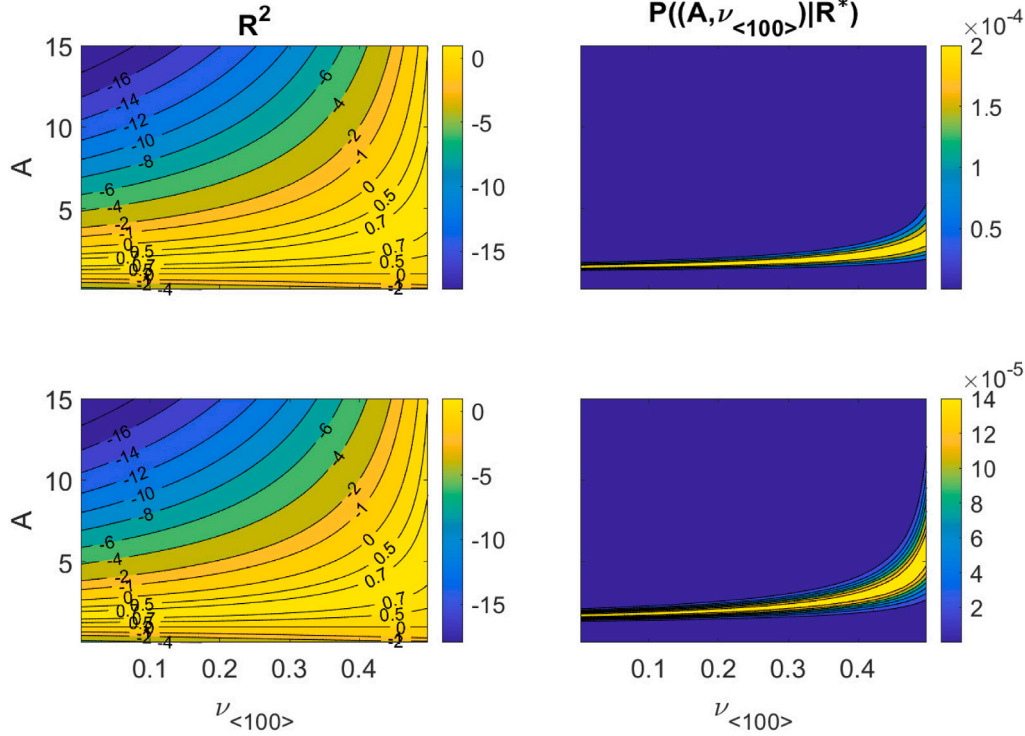


Fig. 5. 2D distributions of the R^2 score and of the posterior probability $P((A, \nu_{\langle 100 \rangle}) | R^*)$ for $\sigma_{E^*} = 50$ GPa with respect to A and $\nu_{\langle 100 \rangle}$ for the Ni (top) and IN718 (bottom) samples.

5.2. Results from Bayesian inference simulations

In the following, Bayesian inference simulation results are presented, starting with Fig. 5 which shows the 2D distributions of the R^2 score (Eq. (23)) and of the posterior probability $P((A, \nu_{\langle 100 \rangle}) | R^*)$ for $\sigma_{E^*} = 50$ GPa. These two distributions exhibit pretty similar shapes and the trend is also alike between Ni and IN718 samples. From these contour plots, a majority of $(A, \nu_{\langle 100 \rangle})$ couples appear out of the realm of possibility because of negative R^2 score or insignificant posterior probability. However, the shape of the high probability or high R^2 score area (e.g., $R^2 > 0.7$) is not concentric. Hence, if the range of likely A values is clearly restricted, it is noteworthy that the whole spectrum of $\nu_{\langle 100 \rangle}$ values can be associated with a high posterior probability or a high R^2 score. This shows the difficulty to choose the most relevant values for A and $\nu_{\langle 100 \rangle}$ just from the computation of the R^2 score when a clear and well-defined minimum does not emerge. Fortunately, it is possible to compute the marginal posterior distributions of A and $\nu_{\langle 100 \rangle}$ by summation of $P((A, \nu_{\langle 100 \rangle}) | R^*)$ for fixed values of A or $\nu_{\langle 100 \rangle}$. Figs. 6, 7, 8 and 9 illustrate some of these marginal posterior distributions at different values of σ_{E^*} . The marginal posterior distributions of A have all well-defined peaks but with some asymmetry.

The marginal posterior distributions of $\nu_{\langle 100 \rangle}$ are completely different with strong asymmetric shapes and exhibit, almost always, a saturation of the maximum probability at the limit of 0.5. Moreover, Figs. 10 and 11 exhibit examples of the posterior probability distributions of $E_{\langle 100 \rangle}$ at different values of σ_{E^*} (see Section 4.2 for the details of the calculation). Once again, these distributions are not symmetric but the asymmetry decreases with the increase of σ_{E^*} .

Finally, the evolution with σ_{E^*} of the MAP (maximum a posteriori), median and mean values of the posterior probability distributions of A , $\nu_{\langle 100 \rangle}$ and $E_{\langle 100 \rangle}$ are displayed in Fig. 12. For comparison, the values of A and $\nu_{\langle 100 \rangle}$ corresponding to the maximum R^2 score and to the maximum of $P((A, \nu_{\langle 100 \rangle}) | R^*)$ are indicated as well. It is seen that the median values of the posterior distributions of A , $\nu_{\langle 100 \rangle}$ and $E_{\langle 100 \rangle}$ always stabilize very well with the increase of σ_{E^*} , while the mean values stabilize well for $\nu_{\langle 100 \rangle}$ and $E_{\langle 100 \rangle}$ but increase with σ_{E^*} for A . The MAP values also increase with σ_{E^*} for A but decrease for $E_{\langle 100 \rangle}$ and saturate at 0.5 for $\nu_{\langle 100 \rangle}$. Regarding this last point, it is important to underline that a value of $\nu_{\langle 100 \rangle} = 0.5$ provides a high value of the posterior probability $P((A, \nu_{\langle 100 \rangle}) | R^*)$ only in association with very high values of A (see Fig. 5). Such high values ($A > 4$) are definitively unrealistic considering the marginal posterior distributions of A (see

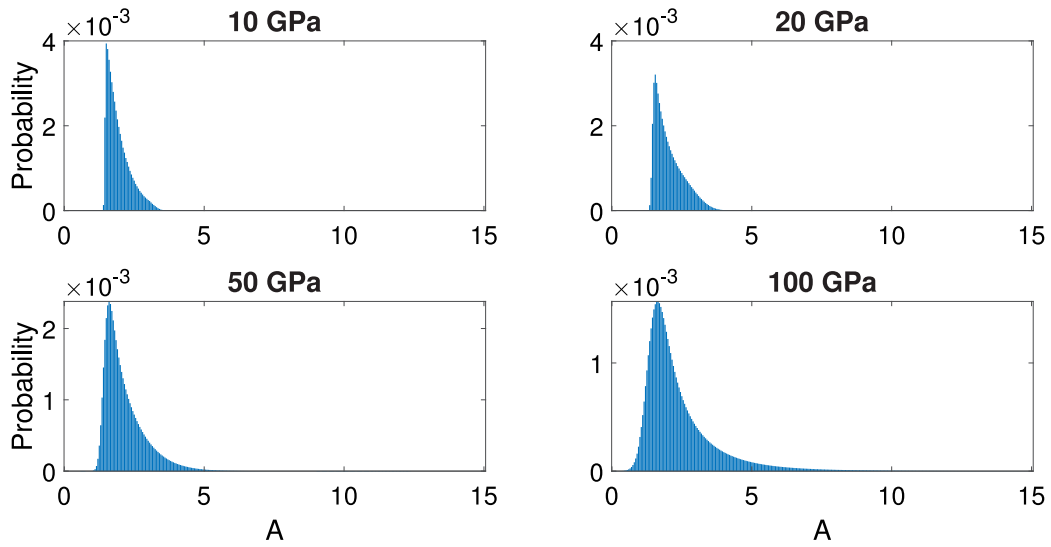


Fig. 6. Marginal posterior distributions of A at 4 different values of σ_{E^*} for the Ni sample.

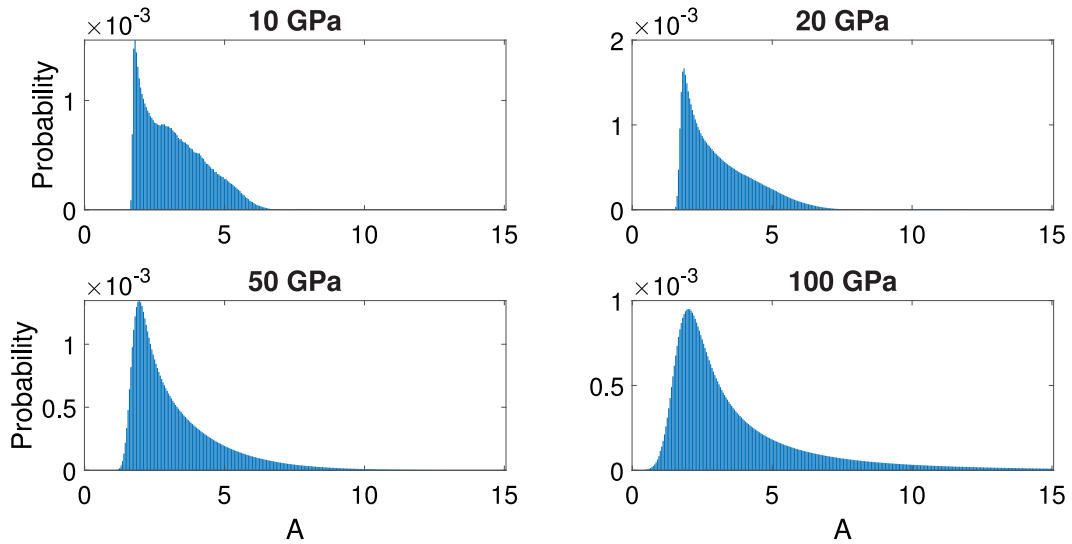


Fig. 7. Marginal posterior distributions of A at 4 different values of σ_{E^*} for the IN718 sample.

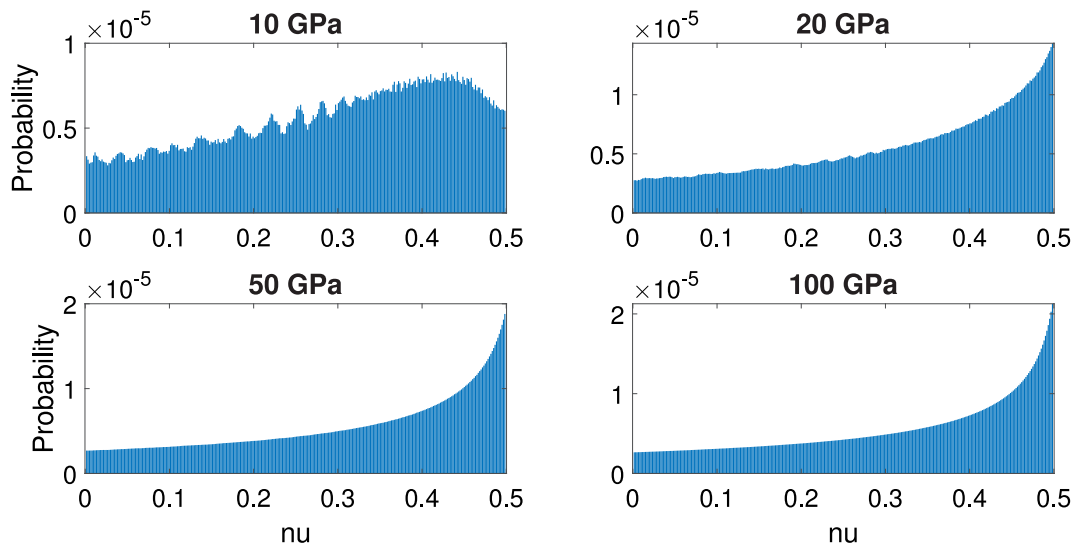


Fig. 8. Marginal posterior distributions of $\nu_{(100)}$ at 4 different values of σ_{E^*} for the Ni sample.

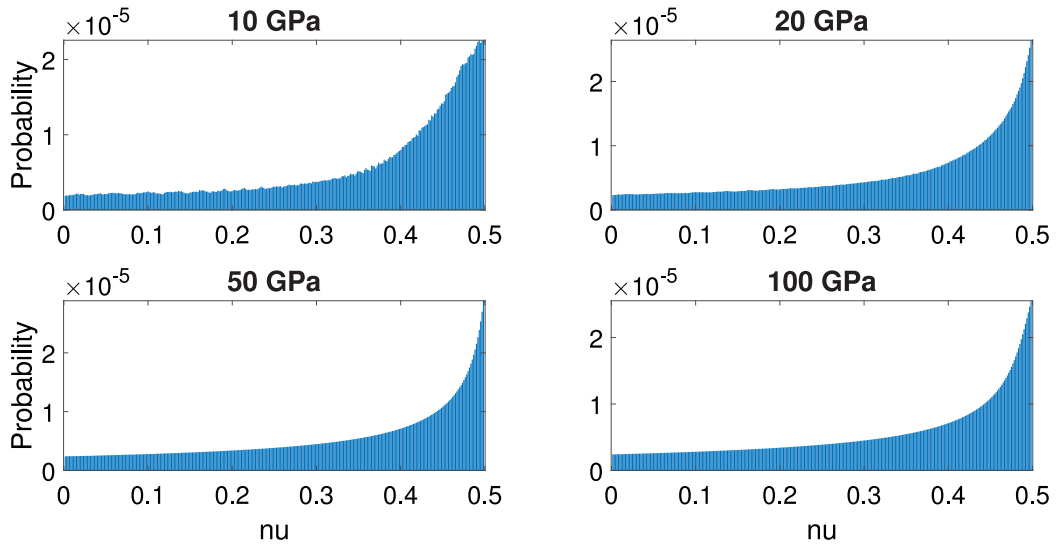


Fig. 9. Marginal posterior distributions of $\nu_{(100)}$ at 4 different values of σ_{E_*} for the IN718 sample.

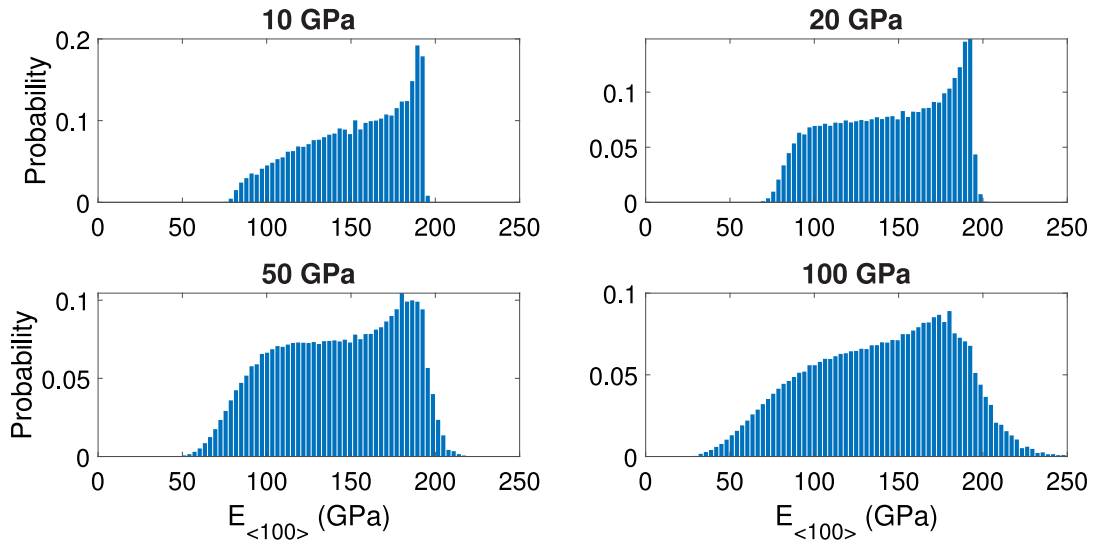


Fig. 10. Posterior probability distributions of $E_{(100)}$ at 4 different values of σ_{E_*} for the Ni sample.

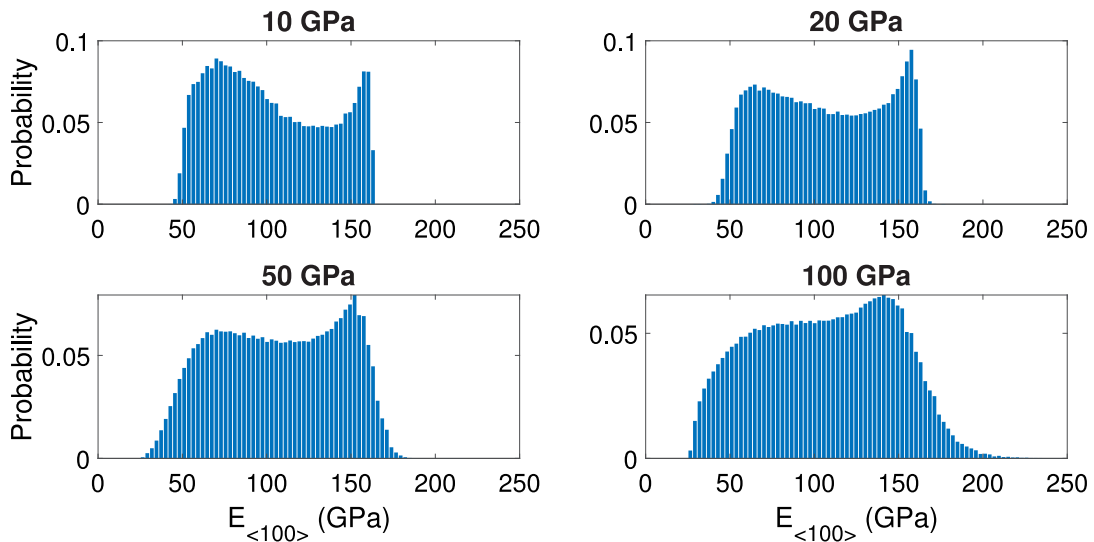


Fig. 11. Posterior probability distributions of $E_{(100)}$ at 4 different values of σ_{E_*} for the IN718 sample.

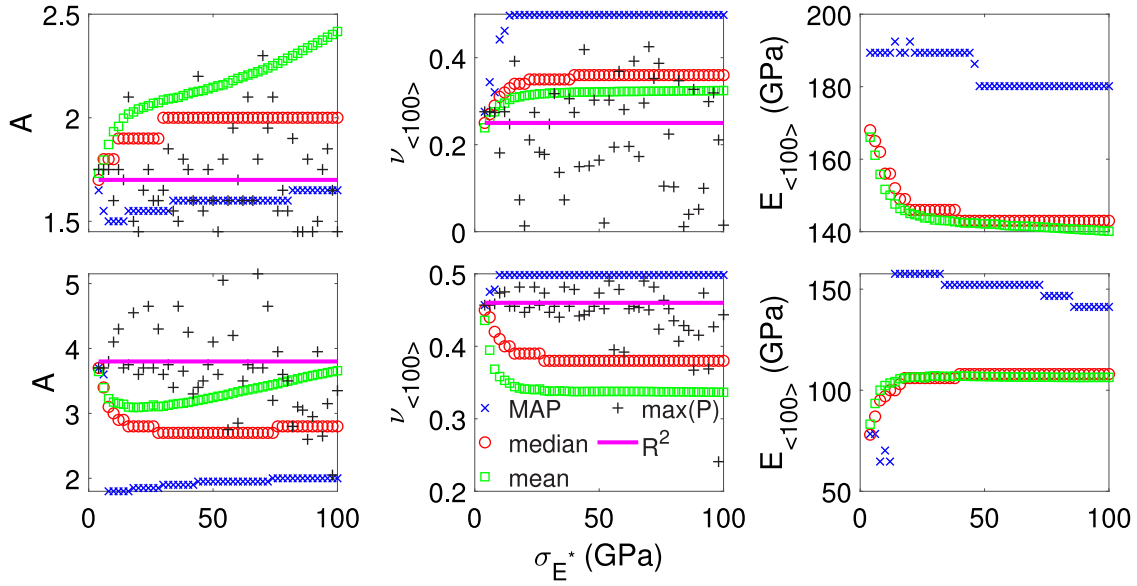


Fig. 12. For the Ni (top) and IN718 (bottom) samples, evolution with σ_{E^*} of the MAP, median and mean values of the marginal posterior distributions of A and $v_{(100)}$, along with the values of A and $v_{(100)}$ associated to the maximum of $P((A, v_{(100)}) | R^*)$ (max(P)) and the ones corresponding to the maximum R^2 score. The evolution of the MAP, median and mean values of the posterior probability distributions of $E_{(100)}$ are shown as well.

Figs. 6 and 7) or the literature range (see further Tables 2 and 3). It is also observed that considering directly the values of A and $v_{(100)}$ associated to the maximum posterior probability $P((A, v_{(100)}) | R^*)$ does not lead to consistent results since strong variations occur when varying σ_{E^*} (see Fig. 12).

Hence, from all the above considerations, it seems well justified to consider the stabilized median values of the posterior distributions of A , $v_{(100)}$ and $E_{(100)}$ as the final retained values. The latter are displayed in Tables 2 and 3 for Ni and IN718 samples, respectively, and correspond to the median values taken at $\sigma_{E^*} = 50$ GPa since no or very little variations are observed after this value (see Fig. 12).

6. Discussion

The retained SEC values for high-purity Ni can be compared to those of the literature values present in Table 2. The latter are taken from Ref. [48]. It gathers the main literature values for the SEC of pure Ni measured by different experimental techniques. On the whole, these values show a good agreement. It is seen that the SEC values obtained by the current approach are well within the literature range, although the values of A (2.0) and $v_{(100)}$ (0.36) lie at the lower limit. When performing the conversion in terms of C_{11} , C_{12} and C_{44} values, the match is actually a little bit less good for C_{11} and C_{12} . This is due to the difference between our value of 0.36 for $v_{(100)}$ and the typical literature value around 0.38. Indeed, when $v_{(100)}$ get close to 0.5, C_{11} and C_{12} start to diverge because of the presence of the $(1 - 2v_{(100)})$ term in the denominator of Eq. (15).

The main literature values for the SEC of IN718 are gathered in Table 3. Compared to pure Ni, there are much less data available and much more variability. It should be also emphasized that, contrary to the Ni data, the SEC values correspond to estimations based on indirect methods, with results closely depending on the choice of the micromechanical model [49–51]. The SEC values obtained by our approach are nevertheless well within this literature range. It can be noticed that the value of $E_{(100)}$ (108 GPa) is just a little bit below the minimum of the literature (114 GPa).

Besides, it is noteworthy that the stabilized median values of the posterior distributions are closer to the literature ranges compared to the stabilized mean or MAP values. Moreover, approaches that consider

Table 2

Values of A , $v_{(100)}$ and $E_{(100)}$ (in GPa) retained after the Bayesian inference simulations for high purity Ni and their conversion into C_{11} , C_{12} and C_{44} values (in GPa) (Present study). Comparisons with literature values (found as C_{11} , C_{12} and C_{44} values and converted in terms of A , $v_{(100)}$ and $E_{(100)}$).

Ref.	A	$v_{(100)}$	$E_{(100)}$	C_{11}	C_{12}	C_{44}
Present study	2.0	0.36	143	240	135	105
[52]	2.1	0.37	139	252	151	104
[53]	2.6	0.39	125	250	160	119
[54]	2.6	0.38	131	252	157	123
[55]	2.5	0.38	139	253	152	124
[42]	2.4	0.39	120	244	158	102
[56]	2.5	0.38	131	247	152	121
[2]	2.5	0.38	130	243	149	119
[57]	2.1	0.40	120	255	169	90
[58]	2.5	0.38	132	246	150	121
[59]	2.5	0.37	139	251	150	124
[60]	2.5	0.38	135	251	153	124
[61]	2.6	0.38	130	248	154	124
[62]	2.4	0.37	141	247	144	124
[63]	2.5	0.38	135	252	154	122
[64]	2.3	0.39	148	288	181	124

Table 3

Values of A , $v_{(100)}$ and $E_{(100)}$ (in GPa) retained after the Bayesian inference simulations for Inconel 718 and their conversion into C_{11} , C_{12} and C_{44} values (in GPa) (Present study). Comparisons with literature values (found as C_{11} , C_{12} and C_{44} values and converted in terms of A , $v_{(100)}$ and $E_{(100)}$).

Ref.	A	$v_{(100)}$	$E_{(100)}$	C_{11}	C_{12}	C_{44}
Present study	2.7	0.38	108	202	124	106
[50]	2.7	0.41	114	260	179	110
[51]	2.4	0.35	124	201	109	110
[49]	2.0	0.36	141	242	139	104

directly the best couple of $(A, v_{(100)})$, from either the maximum posterior probability $P((A, v_{(100)}) | R^*)$ or the maximum R^2 score, provide results which are in general very far from the literature ranges (see Fig. 12). The choice to consider the median values of the marginal posterior distributions seems thus well-justified from both the non-symmetric shapes of the probability distributions, the stabilization of the three SEC with σ_{E^*} and the comparisons with the literature data.

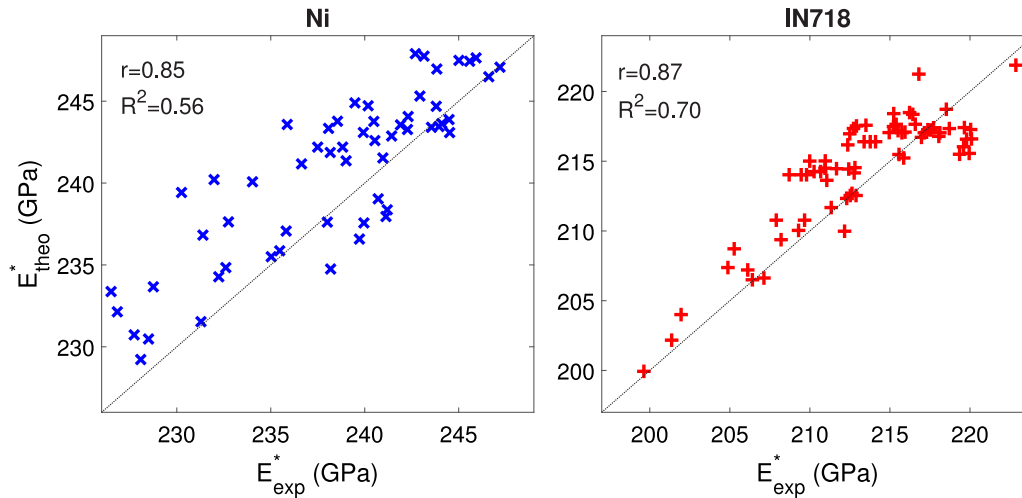


Fig. 13. Indentation moduli E_{theo}^* computed with the Vlassak and Nix's model using the corrective multiplicative factor of 1.06 and the retained values for A , $\nu_{(100)}$ and $E_{(100)}$ in Tables 2 and 3 versus the experimental indentation moduli E_{exp}^* (average per grain). r denotes the Pearson correlation coefficient while the R^2 score corresponds to the coefficient of determination.

Next, it should be underlined that if the present results were obtained by performing HSNM, the latter is not crucial for the success of the method. The proposed procedure should work as well with conventional nanoindentation experiments. Numerical studies based on artificial data show, for instance, that having 4 indents per grain in a set of about 20 grains carefully selected to cover different areas of the IPF map (Fig. 4) should be sufficient to get accurate results depending on the elastic anisotropy of the investigated material. In fact, the method does not necessarily work better if more data are considered. By increasing the number of input data, the probability of having outliers is also increased. A few outliers are however enough to influence the final results in the wrong direction, as can be inferred from the multiplication of individual probabilities to get the likelihood (Eq. (21)). The big advantage of HSNM lies in the possibility to visualize directly how relevant are the input data by comparing EBSD and indentation modulus maps, as done in Fig. 3. Considering this aspect, it may be conjectured that the analysis made for the IN718 sample is certainly more reliable than the one made for the Ni sample, given the much better match between EBSD and E^* maps while the two materials have close elastic anisotropy. The lesser accuracy of the input data for the Ni sample might be the source of the small underestimation of A and $\nu_{(100)}$ values. On the contrary, the good accuracy of the input data for the IN718 sample provides some trust in the SEC values found by our approach (Table 3). This is corroborated by the results of Fig. 13 where the indentation moduli computed with the Vlassak and Nix's model using the retained values for A , $\nu_{(100)}$ and $E_{(100)}$ in Tables 2 and 3 are plotted with respect to the experimental indentation moduli. Both the Ni and IN718 samples exhibit high values of the Pearson correlation coefficient with $r = 0.85$ and $r = 0.87$, respectively. Such a strong positive correlation indicate that the Vlassak and Nix's model capture very well the variation of E^* with the crystallographic orientation of the indentation surface. However, it can be noticed that the R^2 score, herein computed directly from the indentation moduli and not from the ratios as in Fig. 5, is much higher for the IN718 sample ($R^2 = 0.70$) than for the Ni sample ($R^2 = 0.56$). This should be related to the stronger scatter of the Ni data as can be seen from the larger width of the points cloud distribution. Indeed, considering close grain orientations, the measured indentation moduli can sometimes be very different whereas any physical model will predict close values. This issue unavoidably leads to errors between predictions and observations and justify the

need to adopt a statistical approach as the Bayesian inference to handle the experimental uncertainties.

Accordingly, given the reliability of our experimental measurements for the IN718 sample and the good match with the Vlassak and Nix's model, the SEC obtained by the present approach could serve as reference for future studies, especially considering the few, and not totally reliable, data currently available in the literature [49–51]. It is important also to notice that if indents in carbides were systematically removed, the presence of the small and narrowly distributed precipitates, $L1_2\text{-}\gamma'\text{-Ni}_3(\text{Ti,Al})$ and $\text{DO}_{22}\text{-}\gamma''\text{-Ni}_3\text{Nb}$, cannot be excluded from the indented volumes. Hence, the SEC found for the IN718 sample should be interpreted as effective elastic constants that include the effect of these precipitates.

Regarding the use of the Vlassak and Nix's model with a Berkovich tip, it must be noticed that the value of the corrective factor of 1.06 has no influence on the distributions of A and $\nu_{(100)}$ since the method is based on E^* ratios. However, the value of this corrective factor may affect the posterior distributions of $E_{(100)}$. Moreover, it is noteworthy that the orientation of the Berkovich tip in the indentation surface is not considered in the current model. This can create some uncertainties and might explain the need to consider relatively high values of σ_{E^*} in the Bayesian inference simulations to reach convergence. Indeed, increasing the experimental variances lead to an overlapping with a larger set of possible theoretical values, thereby improving the inclusivity of the model. As mentioned in Section 3, the Vlassak and Nix's model should actually represent a better approximation of E^* values obtained by spherical indentation tests even though the contact area is still, in general, not circular but elliptic due to anisotropic elasticity and though a real tip is never perfectly spherical either.

7. Conclusions

In the present study, a novel protocol is presented that couples high-speed nanoindentation mapping (HSNM) with the Vlassak and Nix's model and Bayesian inference simulations to statistically estimate the elastic constants of cubic materials. The originality lies in considering ratios of indentation modulus E^* as input data. Indeed, for cubic elasticity, such ratios just depend on two dimensionless parameters which can be chosen as the Zener ratio A and the directional Poisson's ratio $\nu_{(100)}$. Consequently, we have developed an original Bayesian inference protocol that considers indentation modulus ratios as inputs

and varies only the values of A and $\nu_{\langle 100 \rangle}$. This approach has many advantages:

- The computation time is greatly reduced by considering two constants instead of three. In addition, the use of an optimized Vlassak and Nix's model based on Stroh matrix formalism providing instantaneous results avoids the need to develop surrogate models based on finite element simulations.
- The use of indentation modulus ratios increases the number of data and mitigates the influence of the various calibration parameters on A and $\nu_{\langle 100 \rangle}$.
- The limits of $\nu_{\langle 100 \rangle}$ and the lower limit of A are well-known from elastic stability conditions and are material's independent. Furthermore, the upper limit of A can be easily conjectured unlike the bounds of C_{ij} constants which are much harder to estimate *a priori* for an unknown material.
- The efficiency of the method allows for continuous variation of the uncertainty considered for the experimental moduli. Hence, stabilized Bayesian inference results can be obtained which simplifies the choice of the finally retained values.

Supported by its successful application on high-purity Ni and Inconel 718, we think that the present approach has great potential to investigate the single crystal elastic constants of ill-known cubic phases of multiphase polycrystalline materials. We also think that the general concept of dealing with indentation modulus ratios could be generalized to materials with other symmetry, like transverse isotropy, because the fact that any pre-factor of the stiffness tensor is also a pre-factor of E^* from the Vlassak and Nix's model (cf. Eq. (5)) is not dependent on material's symmetry.

CRedit authorship contribution statement

Y. Idrissi: Writing – original draft, Visualization, Software, Methodology, Investigation, Data curation. **T. Richeton:** Writing – original draft, Visualization, Validation, Supervision, Software, Project administration, Methodology, Investigation, Funding acquisition, Formal analysis, Conceptualization. **D. Texier:** Writing – review & editing, Visualization, Software, Resources, Methodology, Investigation, Funding acquisition, Data curation. **S. Berbenni:** Writing – review & editing, Validation, Software, Methodology. **J.-S. Lecomte:** Writing – review & editing, Visualization, Supervision, Resources, Project administration, Methodology, Investigation, Funding acquisition.

Declaration of competing interest

The authors declare that they have no known competing financial interests or personal relationships that could have appeared to influence the work reported in this paper.

Acknowledgments

This research is supported by the French State through a program operated by the National Research Agency (ANR) "Investment in the future" referenced by ANR-11-LABX-0008-01 (Laboratory of Excellence "DAMAS": Design of Alloy Metals for low-mAss Structures). YI, TR, SB and JSL also acknowledge the experimental facilities MicroMat from LEM3 (Université de Lorraine - CNRS UMR 7239), as well as the use of the Cassiopee Arts et Métiers Institute of Technology HPC Center made available for conducting the research reported in this paper. This work was partly supported by the European Research Council [project HT-S₄DefOx - Grant number 948007].

Appendix. Writing of the cubic stiffness tensor with respect to A , $\nu_{\langle 100 \rangle}$ and $E_{\langle 100 \rangle}$

In the crystal's coordinates system and using Voigt notation, the cubic compliance matrix S writes classically as:

$$S = \begin{bmatrix} S_{11} & S_{12} & S_{12} & 0 & 0 & 0 \\ S_{12} & S_{11} & S_{12} & 0 & 0 & 0 \\ S_{12} & S_{12} & S_{11} & 0 & 0 & 0 \\ 0 & 0 & 0 & S_{44} & 0 & 0 \\ 0 & 0 & 0 & 0 & S_{44} & 0 \\ 0 & 0 & 0 & 0 & 0 & S_{44} \end{bmatrix} \quad (\text{A.1})$$

Considering a uniaxial test along the $\langle 100 \rangle$ crystallographic direction and a linear elastic generalized Hooke's law, we have then:

$$\varepsilon_1 = S_{11}\sigma_1 \text{ and } \varepsilon_2 = S_{12}\sigma_1 \quad (\text{A.2})$$

By definition, the $\langle 100 \rangle$ Young's modulus and the $\langle 100 \rangle$ Poisson's ratio are given by:

$$E_{\langle 100 \rangle} = \frac{\sigma_1}{\varepsilon_1} = \frac{1}{S_{11}} \text{ and } \nu_{\langle 100 \rangle} = -\frac{\varepsilon_2}{\varepsilon_1} = -\frac{S_{12}}{S_{11}} \quad (\text{A.3})$$

In addition, the Zener ratio A is defined as the ratio of μ'' over μ' , the $\{001\}\langle 100 \rangle$ and $\{001\}\langle 110 \rangle$ shear resistances of the crystal (e.g., see [46]):

$$A = \frac{\mu''}{\mu'} \quad (\text{A.4})$$

$$\text{with } \mu' = \frac{1}{2(S_{11} - S_{12})} \text{ and } \mu'' = \frac{1}{S_{44}}$$

From these definitions, we can re-write S as:

$$S = \frac{1}{E_{\langle 100 \rangle}} \times \begin{bmatrix} 1 & -\nu_{\langle 100 \rangle} & -\nu_{\langle 100 \rangle} & 0 & 0 & 0 \\ -\nu_{\langle 100 \rangle} & 1 & -\nu_{\langle 100 \rangle} & 0 & 0 & 0 \\ -\nu_{\langle 100 \rangle} & -\nu_{\langle 100 \rangle} & 1 & 0 & 0 & 0 \\ 0 & 0 & 0 & \frac{2(1 + \nu_{\langle 100 \rangle})}{A} & 0 & 0 \\ 0 & 0 & 0 & 0 & \frac{2(1 + \nu_{\langle 100 \rangle})}{A} & 0 \\ 0 & 0 & 0 & 0 & 0 & \frac{2(1 + \nu_{\langle 100 \rangle})}{A} \end{bmatrix} \quad (\text{A.5})$$

since $\mu' = \frac{E_{\langle 100 \rangle}}{2(1 + \nu_{\langle 100 \rangle})}$. By inverting S , the expression of Eq. (15) for the cubic stiffness matrix C is finally obtained.

References

- [1] H. McSkimin, Measurement of elastic constants at low temperatures by means of ultrasonic waves—data for silicon and germanium single crystals, and for fused silica, *J. Appl. Phys.* 24 (8) (1953) 988–997.
- [2] J. De Klerk, M. Musgrave, Internal conical refraction of transverse elastic waves in a cubic crystal, *Proc. Phys. Soc. Sect. B* 68 (2) (1955) 81.
- [3] S. Matthies, H. Priesmeyer, M. Daymond, On the diffractive determination of single-crystal elastic constants using polycrystalline samples, *J. Appl. Crystallogr.* 34 (5) (2001) 585–601.
- [4] J. Cho, D. Dye, K. Conlon, M. Daymond, R. Reed, Intergranular strain accumulation in a near-alpha titanium alloy during plastic deformation, *Acta Mater.* 50 (19) (2002) 4847–4864.
- [5] D. Delbergue, D. Texier, M. Lévesque, P. Bocher, Diffracting-grain identification from electron backscatter diffraction maps during residual stress measurements: A comparison between the $\sin^2\Phi$ and $\cos\alpha$ methods, *J. Appl. Crystallogr.* 52 (4) (2019) 828–843, <http://dx.doi.org/10.1107/S1600576719008744>.
- [6] S. Fréour, D. Gloaguen, M. François, R. Guillen, E. Girard, J. Bouillo, Determination of the macroscopic elastic constants of a phase embedded in a multiphase polycrystal-application to the β -phase of a Ti-17 titanium based alloy, in: *Materials Science Forum*, Vol. 404, 2002, pp. 723–728.
- [7] S. Fréour, D. Gloaguen, M. François, A. Perronnet, R. Guillén, Determination of single-crystal elasticity constants in a cubic phase within a multiphase alloy: X-ray diffraction measurements and inverse-scale transition modelling, *J. Appl. Crystallogr.* 38 (1) (2005) 30–37.

- [8] S. Raghunathan, A. Stapleton, R. Dashwood, M. Jackson, D. Dye, Micromechanics of Ti-10V-2Fe-3Al: In situ synchrotron characterisation and modelling, *Acta Mater.* 55 (20) (2007) 6861–6872.
- [9] R.r.p. Purushottam raj purohit, T. Richeton, S. Berbenni, L. Germain, N. Gey, T. Connolly, O. Castelnaud, Estimating single-crystal elastic constants of polycrystalline β metastable titanium alloy: A Bayesian inference analysis based on high energy X-ray diffraction and micromechanical modeling, *Acta Mater.* 208 (2021) 116762.
- [10] T. Li, Y. Gao, H. Bei, E.P. George, Indentation schmid factor and orientation dependence of nanoindentation pop-in behavior of NiAl single crystals, *J. Mech. Phys. Solids* 59 (6) (2011) 1147–1162.
- [11] C. Caer, E. Patoor, S. Berbenni, J.-S. Lecomte, Stress induced pop-in and pop-out nanoindentation events in CuAlBe shape memory alloys, *Mater. Sci. Eng.: A* 587 (2013) 304–312.
- [12] J. Weaver, M. Priddy, D. McDowell, S. Kalidindi, On capturing the grain-scale elastic and plastic anisotropy of alpha-Ti with spherical nanoindentation and electron back-scattered diffraction, *Acta Mater.* 117 (2016) 23–34, <http://dx.doi.org/10.1016/j.actamat.2016.06.053>.
- [13] P. Fernandez-Zelaia, V.R. Joseph, S.R. Kalidindi, S.N. Melkote, Estimating mechanical properties from spherical indentation using Bayesian approaches, *Mater. Des.* 147 (2018) 92–105.
- [14] A. Castillo, S.R. Kalidindi, A Bayesian framework for the estimation of the single crystal elastic parameters from spherical indentation stress-strain measurements, *Front. Mater.* 6 (2019) 136.
- [15] J. Everaerts, C. Papadaki, W. Li, A.M. Korsunsky, Evaluation of single crystal elastic stiffness coefficients of a nickel-based superalloy by electron backscattered diffraction and nanoindentation, *J. Mech. Phys. Solids* 131 (2019) 303–312.
- [16] M. Mejri, B. Malard, Y. Thimont, D. Connétable, P. Floquet, R. Laloo, A. Proietti, C. Estournès, Investigation of the mechanical properties of Mn15Si26 via EBSD-nanoindentation coupling and ab-initio calculation, *J. Alloys Compd.* 900 (2022) 163458.
- [17] J. Aspinall, D. Armstrong, M. Pasta, EBSD-coupled indentation: nanoscale mechanics of lithium metal, *Mater. Today Energy* 30 (2022) 101183, <http://dx.doi.org/10.1016/j.mtener.2022.101183>.
- [18] M. Seehaus, S.H. Lee, T. Stollenwerk, J.M. Wheeler, S. Korte-Kerzel, Estimation of directional single crystal elastic properties from nano-indentation by correlation with EBSD and first-principle calculations, *Mater. Des.* 234 (2023) 112296, <http://dx.doi.org/10.1016/j.matdes.2023.112296>.
- [19] D. Texier, T. Richeton, H. Proudhon, A. Dziri, Q. Sirvin, M. Legros, Increase in elastic and hardness anisotropy of titanium with oxygen uptake due to high temperature oxidation: A multimodal framework using high speed nanoindentation mapping, *Mater. Charact.* 216 (2024) 114244, <http://dx.doi.org/10.1016/j.matchar.2024.114244>.
- [20] A. Cazzani, M. Rovati, Extrema of Young's modulus for cubic and transversely isotropic solids, *Int. J. Solids Struct.* 40 (7) (2003) 1713–1744.
- [21] W. Gerberich, J. Nelson, E. Lilleodden, P. Anderson, J. Wyrobek, Indentation induced dislocation nucleation: The initial yield point, *Acta Mater.* 44 (9) (1996) 3585–3598, [http://dx.doi.org/10.1016/1359-6454\(96\)00010-9](http://dx.doi.org/10.1016/1359-6454(96)00010-9).
- [22] F. Habiyaemye, A. Guitton, X. Chen, T. Richeton, S. Berbenni, F. Schäfer, G. Laplanche, N. Maloufi, Influence of pre-existing configurations of dislocations on the initial pop-in load during nanoindentation in a CrCoNi medium-entropy alloy, *Phil. Mag.* 104 (3) (2024) 137–160, <http://dx.doi.org/10.1080/14786435.2023.2290541>.
- [23] J. Vlassak, W.D. Nix, Indentation modulus of elastically anisotropic half spaces, *Philos. Mag.* A 67 (5) (1993) 1045–1056, <http://dx.doi.org/10.1080/01418619308224756>.
- [24] J. Vlassak, W. Nix, Measuring the elastic properties of anisotropic materials by means of indentation experiments, *J. Mech. Phys. Solids* 42 (8) (1994) 1223–1245, [http://dx.doi.org/10.1016/0022-5096\(94\)90033-7](http://dx.doi.org/10.1016/0022-5096(94)90033-7).
- [25] J. Vlassak, M. Ciavarella, J. Barber, X. Wang, The indentation modulus of elastically anisotropic materials for indenters of arbitrary shape, *J. Mech. Phys. Solids* 51 (9) (2003) 1701–1721, [http://dx.doi.org/10.1016/S0022-5096\(03\)00066-8](http://dx.doi.org/10.1016/S0022-5096(03)00066-8).
- [26] D. Barnett, J. Lothe, Line force loadings on anisotropic half-spaces and wedges, *Phys. Nor.* 8 (1975) 13–22.
- [27] A. Stroh, Dislocations and cracks in anisotropic elasticity, *Philos. Mag.* 3 (30) (1958) 625–646.
- [28] T. Zhu, J. Li, K.J. Van Vliet, S. Ogata, S. Yip, S. Suresh, Predictive modeling of nanoindentation-induced homogeneous dislocation nucleation in copper, *J. Mech. Phys. Solids* 52 (3) (2004) 691–724.
- [29] G. Ziegenhain, H.M. Urbassek, A. Hartmaier, Influence of crystal anisotropy on elastic deformation and onset of plasticity in nanoindentation: A simulation study, *J. Appl. Phys.* 107 (6) (2010).
- [30] E. Rossi, J.M. Wheeler, M. Sebastiani, High-speed nanoindentation mapping: A review of recent advances and applications, *Curr. Opin. Solid State Mater. Sci.* (2023) 101107.
- [31] D. Texier, D. Monceau, J.-C. Salabura, R. Mainguy, E. Andrieu, Micromechanical testing of ultrathin layered material specimens at elevated temperature, *Mater. High Temp.* 33 (4–5) (2016) 325–337, <http://dx.doi.org/10.1080/09603409.2016.1182250>.
- [32] R. Hielscher, H. Schaeben, A novel pole figure inversion method: Specification of the MTEX algorithm, *J. Appl. Crystallogr.* 41 (6) (2008) 1024–1037, <http://dx.doi.org/10.1107/S0021889808030112>.
- [33] A. Marano, C. Ribart, H. Proudhon, Towards a data platform for multimodal 4D mechanics of material microstructures, *Mater. Des.* In press (2024) 113306, <http://dx.doi.org/10.1016/j.matdes.2024.113306>.
- [34] H. Proudhon, T. Richeton, D. Texier, A. Dziri, Q. Sirvin, M. Legros, Correlative analysis of EBSD and high speed nanoindentation mapping datasets in pure titanium, 2024, <http://dx.doi.org/10.5281/zenodo.10842559>.
- [35] Y.-T. Cheng, W. Ni, C.-M. Cheng, Nonlinear analysis of oscillatory indentation in elastic and viscoelastic solids, *Phys. Rev. Lett.* 97 (7) (2006) 075506.
- [36] M.R. VanLandingham, Review of instrumented indentation, *J. Res. Natl. Inst. Stand. Technol.* 108 (4) (2003) 249.
- [37] I.N. Sneddon, The relation between load and penetration in the axisymmetric boussinesq problem for a punch of arbitrary profile, *Internat. J. Engrg. Sci.* 3 (1) (1965) 47–57, [http://dx.doi.org/10.1016/0020-7225\(65\)90019-4](http://dx.doi.org/10.1016/0020-7225(65)90019-4).
- [38] T. Timoshenko, J. Goodier, *Theory of Elasticity*, second ed., McGraw-Hill, N.Y., 1951.
- [39] D. Bacon, D. Barnett, R.O. Scattergood, Anisotropic continuum theory of lattice defects, *Prog. Mater. Sci.* 23 (1980) 51–262.
- [40] T. Ting, Image singularities of Green's functions for anisotropic elastic half-spaces and bimetals, *Quart. J. Mech. Appl. Math.* 45 (1) (1992) 119–139.
- [41] J. Yin, D.M. Barnett, W. Cai, Efficient computation of forces on dislocation segments in anisotropic elasticity, *Modelling Simul. Mater. Sci. Eng.* 18 (4) (2010) 045013.
- [42] M. Yamamoto, On elastic constants of nickel crystals, *Phys. Rev.* 77 (4) (1950) 566.
- [43] G. D'Agostini, Bayesian inference in processing experimental data: principles and basic applications, *Rep. Progr. Phys.* 66 (9) (2003) 1383.
- [44] H. Rappel, L.A. Beex, S.P. Bordas, Bayesian inference to identify parameters in viscoelasticity, *Mech. Time-Depend. Mater.* 22 (2018) 221–258.
- [45] T. Bayes, LII. An essay towards solving a problem in the doctrine of chances. By the late rev. Mr. Bayes, FRS communicated by Mr. Price, in a letter to John Canton, AMFR S, *Philos. Trans. R. Soc. Lond.* (53) (1763) 370–418.
- [46] R. deWit, Elastic constants and thermal expansion averages of a nontextured polycrystal, *J. Mech. Mater. Struct.* 3 (2) (2008) 195–212.
- [47] E. Diaz-Francés, F.J. Rubio, On the existence of a normal approximation to the distribution of the ratio of two independent normal random variables, *Statist. Papers* 54 (2013) 309–323.
- [48] H.M. Ledbetter, R.P. Reed, Elastic properties of metals and alloys, I. Iron, nickel, and iron-nickel alloys, *J. Phys. Chem. Ref. Data* 2 (3) (1973) 531–618.
- [49] P. Haldipur, *Material Characterization of Nickel-Based Super Alloys Through Ultrasonic Inspection*, Iowa State University, 2006.
- [50] G. Martin, N. Ochoa, K. Sai, E. Hervé-Luano, G. Cailletaud, A multiscale model for the elastoviscoplastic behavior of directionally solidified alloys: Application to FE structural computations, *Int. J. Solids Struct.* 51 (5) (2014) 1175–1187.
- [51] J. Schröder, A. Heldmann, M. Hofmann, A. Evans, W. Petry, G. Bruno, Determination of diffraction and single-crystal elastic constants of laser powder bed fused inconel 718, *Mater. Lett.* 353 (2023) 135305.
- [52] K. Honda, Y. Shirakawa, On Young's modulus of elasticity of single crystal of nickel, *J. Japan Inst. Met.* 1 (1937) 217–219.
- [53] R. Bozorth, W. Mason, H. McSkimin, J. Walker, Elastic constants and internal loss of single nickel crystals, *Phys. Rev.* 75 (12) (1949) 1954.
- [54] R. Bozorth, W. Mason, H. McSkimin, Frequency dependence of elastic constants and losses in nickel, *Bell Syst. Tech. J.* 30 (4) (1951) 970–989.
- [55] J. Neighbours, F. Bratten, C.S. Smith, The elastic constants of nickel, *J. Appl. Phys.* 23 (4) (1952) 389–393.
- [56] S. Levy, R. Truell, Ultrasonic attenuation in magnetic single crystals, *Rev. Modern Phys.* 25 (1) (1953) 140.
- [57] Y. Shirakawa, K. Numakura, Elasticity constants of single crystals of nickel-copper alloys, *Sci. Rep. Res. Inst. Tohoku Univ. Ser. A* 10 (1958) 51–57.
- [58] J. De Klerk, Ultrasonic wave propagation in a nickel single crystal, *Proc. Phys. Soc.* 73 (3) (1959) 337.
- [59] G. Alers, J. Neighbours, H. Sato, Temperature dependent magnetic contributions to the high field elastic constants of nickel and an Fe-Ni alloy, *J. Phys. Chem. Solids* 13 (1–2) (1960) 40–55.
- [60] J. Sakurai, M. Fujii, Y. Nakamura, H. Takaki, Elastic constants of Ni-Fe and Ni-Cu alloys, *J. Phys. Soc. Japan* 19 (3) (1964) 308–310.
- [61] S. Epstein, O. Carlson, The elastic constants of nickel-copper alloy single crystals, *Acta Metall.* 13 (5) (1965) 487–491.
- [62] E. Vintaikin, X-Ray determination of the elastic constants of pure nickel and its alloy with aluminum, in: *Soviet Physics Doklady*, Vol. 11, 1966, p. 91.
- [63] K. Salama, G. Alers, Third-order elastic moduli of pure nickel and some dilute copper-nickel alloys, *IEEE Trans. Sonics Ultrason.* 1 (1969) 28.
- [64] Y. Shirakawa, Y. Tanji, H. Moriya, I. Oguma, Elastic constants of Ni and Ni-Fe-FCC-alloys, *J. Japan Inst. Met.* 33 (10) (1969) 1196–1202.